www.MaterialsViews.com

ADVANCED OPTICAL MATERIALS
www.advopticalmat.de

FULL PAPER

3D Printed Hollow-Core Terahertz Optical Waveguides with Hyperuniform Disordered Dielectric Reflectors

*Tian Ma, Hichem Guerboukha, Martin Girard, Andrew D. Squires, Roger A. Lewis, and Maksim Skorobogatiy**

Novel hollow-core THz waveguides featuring hyperuniform disordered reflectors are proposed, fabricated, and characterized. The reflector comprises aperiodically positioned dielectric cylinders connected with dielectric bridges. The proposed waveguides are fabricated using a 3D MultiJet printer. Optical properties of the fabricated waveguides are investigated numerically using finite element method, as well as experimentally using terahertz time-domain spectroscopy. The results confirm that proposed waveguides exhibit sizable photonic bandgaps (21%) even with relatively low refractive index contrast (resin/air). Position of the bandgaps can be easily tuned by varying reflector geometrical parameters.

1. Introduction

Photonics crystal (PC) materials have drawn great interest over the years because of their unique properties that allow advanced light management.[1] In particular, dielectric reflectors based on PCs can be employed to create hollow-core fibers by arranging such reflectors around a gas filled cavity. In such fibers, the light is confined in the hollow-core for frequencies within the reflector photonic bandgaps (PBGs). Based on this principle, various hollow-core PBG fibers have been proposed for simultaneously low-loss and low-dispersion guidance over sizable spectral ranges.[2,3] These fibers can be divided into two categories, Bragg fibers and holey fibers, according to their reflector structure.

Generally, hollow-core Bragg fibers consist of a circularly symmetric Bragg reflector, which is formed by alternate high and low refractive index layers. The Bragg reflector can be all-solid or porous. The all-solid Bragg reflector is formed by repeating alternate concentric layers of two different polymers[4] or the same polymer with different dopants.[5,6] The bandgap position and its spectral width are determined by the thickness and the refractive indices of the alternate layers. The periodic refractive index variation in Bragg reflectors can also be realized by introducing rings of porous material. Using this approach, hollow core Bragg fibers with solid/randomly porous multilayers,[7] air-hole rings[8] and cob-web structures[9,10] were investigated in the terahertz range. Another type of hollow core PBG fiber is the holey fiber. Such fiber features reflectors formed by various types of periodic lattices, such as, rectangular,[11] triangular,[11,12] honeycomb,[13] etc. The holey PBG fibers are typically designed to have high air-filling fractions in order to achieve bandgap.

Recently, both numerical[14–16] and experimental[17–20] studies in 2D have shown that hyperuniform disordered structures present a new class of disordered photonics materials that can possess large complete photonic bandgaps for all polarizations. In these studies, the key parameter that characterizes hyperuniform structures is the hyperuniformity χ, which was first introduced as an order metric of a point pattern based on its local density fluctuations.[19] The hyperuniformity is zero for a random pattern taken from a Poisson distribution, which becomes disordered when $\chi > 0$ and eventually settles in a crystal pattern around $\chi \sim 0.8$. A particular type of hyperuniform disordered structure that was considered in[19] comprises dielectric cylinders connected by thin dielectric bridges. Based on this structure, various planar hyperuniform waveguides have been developed with both high[16] and low refractive index contrasts[17] that exhibited spectrally broad bandgaps, as well as photonic bandgap guidance for all polarizations. Moreover, it was demonstrated in[18] that for the same refractive index contrast, hyperuniform reflectors can have larger bandgaps than their counterparts featuring periodic PCs. Thus, it could be expected that hollow-core PBG fibers featuring hyperuniform reflectors could have spectrally broader bandgap than hollow-core PBG fibers that use strictly periodic reflectors.

In this paper, we propose a novel hollow-core terahertz PBG waveguide that uses hyperuniform disordered reflectors. This is essentially a generalization of the earlier 2D waveguides featuring hyperuniform claddings[14–20] into 3D waveguides and fibers. Our main motivation is to explore the possibility of designing hollow-core waveguides that feature spectrally broad

T. Ma, H. Guerboukha, Prof. M. Skorobogatiy
Department of Engineering Physics
École Polytechnique de Montréal
Montreal, Québec H3T 1J4, Canada
E-mail: maksim.skorobogatiy@polymtl.ca

M. Girard
Department of Materials Science and Engineering
Northwest University
Evanston, IL 60208, USA

A. D. Squires, R. A. Lewis
Institute for Superconducting and Electronic Materials
School of Physics
University of Wollongong
NSW 2522, Australia

DOI: 10.1002/adom.201600171

FULL PAPER

bandgaps that are potentially superior to those attainable with purely periodic structures. Particularly, we demonstrate theoretically that using resin/air material combination that offers relatively low refractive index contrast of 1.67/1, one can design a hollow core waveguide featuring a 90 GHz (≈21%) bandgap centered in the vicinity of 0.41 THz. In such waveguide, highly porous PBG reflector is comprised of ≈113 µm radius cylinders connected with ≈35 µm thick bridges. We then fabricate such waveguides using 3D MultiJet printing. The diameter of the resultant waveguides (reflector size) is ≈20 mm, while the diameter of the hollow core is ≈5 mm. Due to limitations in the 3D printing process that we have used, the resolution was limited to 100 µm which allowed us to print structures with bridges thicker than 200 µm. As we demonstrate, both theoretically and experimentally, thicker bridges lead to an overall reduction of the bandgap spectral size. Nevertheless, the fabricated waveguides featured relatively wide bandgaps (up to ≈15%) and low transmission losses (<0.10 cm^{-1}) within their PBGs.

2. Fiber Design

In order to generate a disordered reflector structure, we use a set of dielectric cylinders connected with thin dielectric bridges. The cylinder centers follow a distribution of 2D hyperuniform point pattern. For any point pattern, its point distribution can be characterized by its number variance, which is given by the standard deviation of the number of points (N_R) in a sampling window Ω of radius R in d dimension, $\sigma^2(R) = \langle N_R^2\rangle - \langle N_R\rangle^2$.[21] A point pattern is called "hyperuniform" if the corresponding number variance within Ω grows slower than the volume of Ω namely R^d. In reciprocal space, the point distribution can be characterized by its structure factor $S(k)$. In,[14] it has been shown that if a hyperuniform point pattern is tailored such that its structure factor $S(k)$ is zero for all $|k| < k_c$, such a point pattern is called "stealthy" and can produce photonic bandgaps. Moreover, the critical value k_c can be related to the hyperuniformity χ, which is defined as[20]

$$\chi = \frac{M(k_c)}{d \bullet N} \tag{1}$$

where $M(k_c)$ is the number of constrained degree of freedom and $d \bullet N$ is the total number of degrees of freedom with d is the number of dimensions and N is the total number of points.

In our design, we used a value of $\chi = 0.5$ since it has been shown in[14] that it generates a hyperuniform point pattern that can be optimized to produce a complete PBG for both transverse electric (TE) and transverse magnetic (TM) polarizations in a 2D photonic crystal waveguide. To drive the structure factor $S(k)$ to zero for all $|k| < k_c$, we changed the particle coordinates using the TOMLAB's MINOP algorithm, which is a Fortan-based reduced gradient nonlinear optimization solver. In **Figure 1**a, we illustrate the Fourier transform in the k-space of the generated hyperuniform point pattern. The brightness of each point is proportional to the absolute value of its structure factor $S(k)$.

Then, following the method described in,[14] we developed the cross section of the proposed waveguide based on the generated hyperuniform point pattern. A triangular mesh is defined with the hyperuniform point pattern as its vertices using the Delaunay triangulation method. Then, cylinders with radii of r_c are placed at the centroid of each triangular cell. Finally, cylinders in neighboring triangular cells are connected using dielectric bridges of thickness t_b. The central part of thus generated structure was replaced with a hollow core of 5 mm diameter. The final step in our design was to maximize the full PBG width of the proposed waveguide by optimizing its structural parameters, namely the cylinder radius r_c and the bridge thickness t_b. Similar optimization has been done in,[14] where these structural parameters were optimized for a planar hyperuniform waveguide with the optimized parameters expressed as

$$\begin{aligned} r_c &= \alpha \frac{L}{\sqrt{N}} \\ t_b &= \beta \frac{L}{\sqrt{N}} \end{aligned} \tag{2}$$

where L is the size length of the supercell and N is the number of points in this supercell. For our waveguide, L = 21 mm and N = 256. In our simulation, we set the central frequency of the PBG at 0.4 THz and the cladding material refractive index at 1.67. Then, by performing consecutive sweeps of both α and β parameters, we can iteratively optimize the waveguide structure and maximize the resultant PBG at a fixed frequency. Particularly, at each optimization step, we fix one of the parameters (say α) at the optimal value found in the previous step. Then, we perform a 1D sweep of the other parameter (β) and find its new optimal value. We then repeat the procedure by switching the parameters (fix β, sweep α). Optimal value of a parameter is defined as one that results in an equidistant separation of the air light line from both the lower and the upper edges of the continuum of cladding states. This optimization condition is meant to minimize scattering of the core guided modes (with effective refractive indices close to that of air) into the continuum of cladding modes. After several such iterations the values of the two parameters converge to their optimal values of $\alpha = 0.084$ and $\beta = 0.027$ with the corresponding optimal cylinder radius and bridge thickness being 113 and 35 µm, respectively. In **Figure 2**a,b, we demonstrate two consecutive sweeps of α and β after convergence is achieved. The proposed waveguide with optimized parameters is shown in Figure 1b, and the corresponding band diagram is demonstrated in Figure 2c. The resultant bandgap width is ≈90 GHz.

3. Optical Characterization

3.1. Band Diagram of the Proposed Waveguides

Light guidance in the proposed waveguides was analyzed using commercial finite element software COMSOL. For the experimentally fabricated waveguides, the reflector geometries were extracted from the high resolution photographs of the waveguides cross-sections [see Figure 1c,e]. For the frequency-dependent refractive index and absorption loss of the reflector material, we used polynomial fits (Equations (S2) and

Adv. Optical Mater. 2016, DOI: 10.1002/adom.201600171

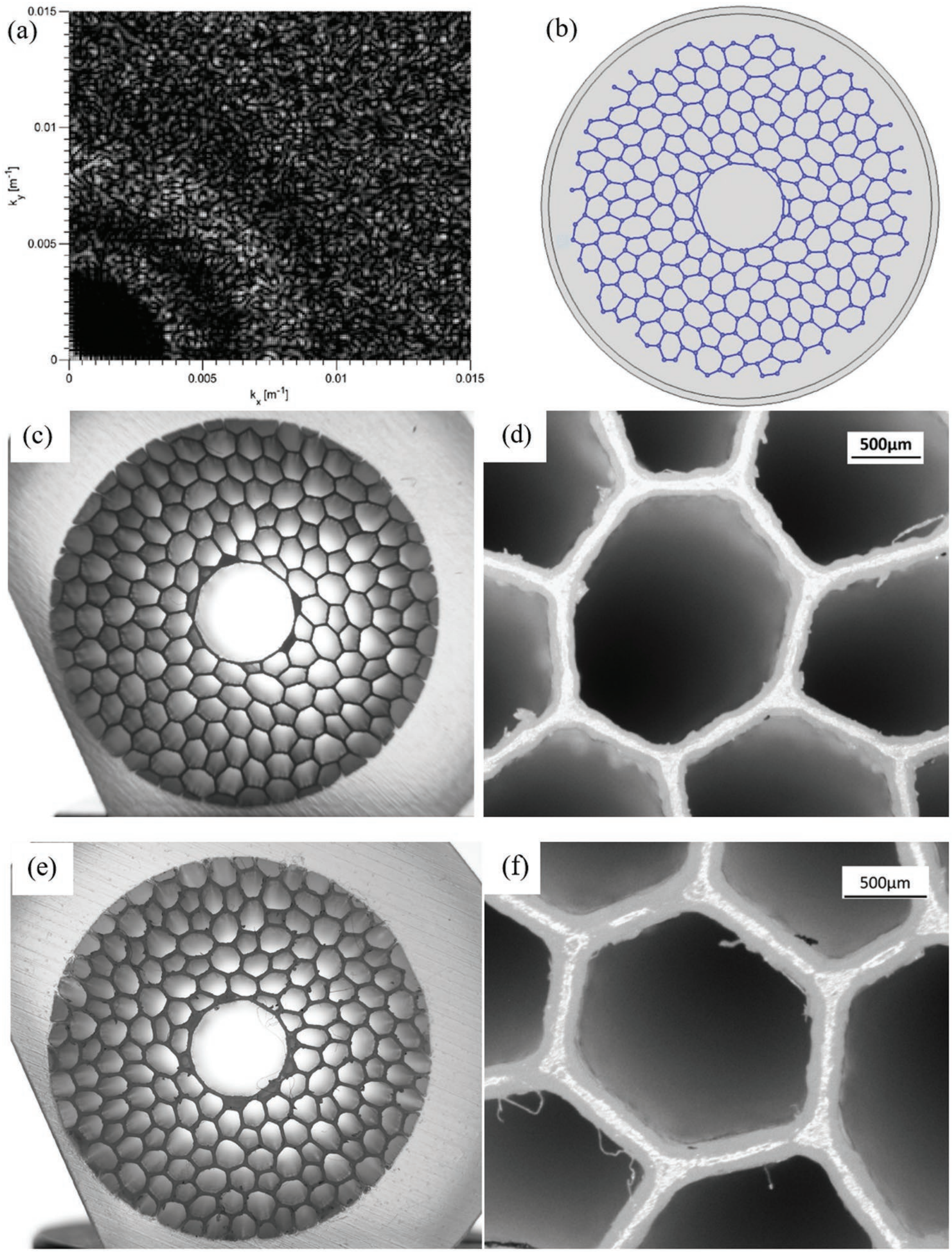

Figure 1. a) Hyperuniform point pattern in k-space. This point pattern is used to define center positions of the dielectric cylinders in the hyperuniform PBG reflector. b) Waveguide and a computational cell used in our numerical simulations. The reflector material is shown in blue, while the air is gray; the computational domain is terminated by a circular perfect electric conductor. The cylinder radii are 113 µm and the bridge thickness is 35 µm. c) The fabricated waveguide with a bridge thickness of 200 µm in the reflector. d) Zoom of the reflector region shown in (c). e) The fabricated waveguide with a bridge thickness of 250 µm. f) Zoom of the reflector region shown in (e).

(S3), Supporting Information) on experimental data presented in Section S1 of the Supporting Information. Computational cell was terminated by a circular perfect electric conducting boundary. Modal dispersion relations of all guided modes for the two fabricated waveguides with different bridge thicknesses are presented in Figure 4c,d. In these band diagrams, we present the modal effective refractive indices (n_{eff}) of the guided modes as a function of frequency in the range of 0.1–0.5 THz. Due to large system size and small features, modal simulation above 0.5 THz is problematic due to time and memory limitations. The color code for the band diagrams (**Figure 3**b and **Figure 4**) indicates the fraction of the power guided by the individual mode within the hollow core. Thus, the blue color refers to modes with power localized mostly outside the waveguide core, while the red color refers to strong presence of the modal fields in the hollow core. In order to show core guided modes clearly, we use bigger dots to represent the modes with more than 60% of the total power in the core. The red solid line in these diagrams is the light line of air with $n = 1$, while the red dashed lines define the edges of the photonic bandgaps.

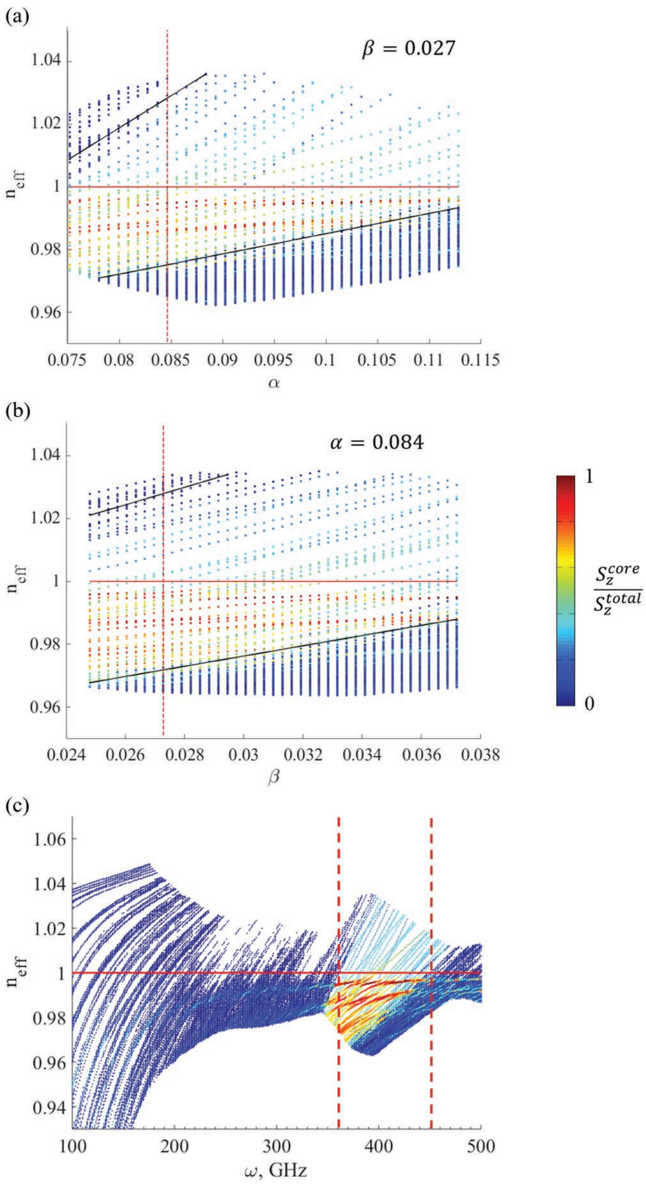

Figure 2. Optimization of the waveguide structure. a) Sweeping α with fixed $\beta = 0.027$ results in an optimal value of $\alpha = 0.084$, while b) sweeping β with fixed $\alpha = 0.084$ results in an optimal value of $\beta = 0.027$. The two black solid lines define the boundaries of the continuum of the cladding-bound states. The red line refers to the air light line with $n = 1$. The red dashed line shows the optimal parameter value for which the air light line is positioned strictly in the middle between the two boundaries with the continuum of cladding states. c) The band diagram of the numerically optimized waveguide structure. The red dashed lines refer to the boundaries of the bandgap centered at 0.41 THz, having the width of ≈90 GHz. The red solid line shows the air light line.

As discussed in Section 2, the numerically optimized reflector structure (r_c = 113 µm, t_b = 35 µm) presents a relatively wide photonic bandgap in the vicinity of 0.4 THz. Here, we investigate in greater detail the band diagram of the numerically optimized structure with and without the hollow core (Figure 3a,b respectively). In the case of the coreless waveguide, COMSOL mode solver finds artificial modes propagating inside the bulk of the reflector structure, as well as spurious modes confined in the vicinity of the boundary. To exclude these spurious modes due to numeric boundary, in Figure 3a we only present the modes that propagate in the bulk of the reflector and that have more than 30% of the total power guided in an area delimited by a radius equal to 2/3 of the waveguide outer boundary. As shown in Figure 3a, the resultant bandgap is centered at 0.41 THz and its width is about ≈75 GHz (see the definition of the bandgap in Section 4). When introducing a hollow core of 5 mm diameter, the bandgap features a plethora of modes that can be further identified as core guided modes and surface states. Thus, the guided modes are presented in Figure 3b with dispersion relations that have red-orange color. Such modes feature fields that are strongly confined (more than 80% by power) in the waveguide hollow core. Even for frequencies outside the bandgap, dispersion relations of the guided modes (or rather resonant modes in this case) can still be clearly identified due to the light blue color of their dispersion relations (20%–40% modal power still remaining in the fiber core) that stand out in the background of the dark blue dispersion relations corresponding to the modes of a reflector. Another type of modes present in the bandgap are the surface states that are confined in the direct vicinity of the fiber core/reflector interface. Dispersion relations of such modes have light blue colors (20%–50% of modal power in the core), and such modes have significant presence both in the fiber core and in the reflector. Spectrum of the surface states is highly sensitive to the structure of the core boundary. Surface states can, in principle, be largely suppressed via a careful design of the fiber core/reflector interface, which is, however, not a focus of this paper. In Figure 3c, we present longitudinal flux (S_z) distributions of several typical modes positioned inside and outside of the PBG at 0.38 THz. Particularly, the core guided modes inside the reflector bandgap, namely the first higher order mode B and the fundamental mode C, are strongly confined in the core region. The modes of the reflector found outside the reflector bandgap (modes A and F in Figure 3b) have strong presence in the cladding region. Finally, surface states within the reflector bandgap (modes D and E) are localized in the vicinity of the hollow core/reflector interface. Additionally, dispersion relations of the surface states can show avoided crossing phenomenon with the dispersion relations of the core guided modes. In the vicinity of the avoided crossing frequency (see red circle in Figure 3b, for example), surface states can be strongly coupled (hybridized) with the core guided modes, thus affecting guided mode dispersion relations and losses. This phenomenon is further detailed in Section 4.

We also note that upon closer inspection, most dispersion relations corresponding to the core guided modes are made, in fact, of two nearly degenerate dispersion relations. This near degeneracy comes from the fact that the hollow core boundary is circular, while the core diameter (5 mm) is much larger than the operation wavelength (≈0.75 mm at 0.4 THz). Here, we would like to remind the reader that in the circularly symmetric hollow-core fibers,[22] most of the guided modes are doubly degenerated. In the case of the hyperuniform reflector, the modal degeneracy is lifted due to noncircularly symmetric structure of the reflector. Intermodal birefringence, however, remains very small due to low presence of the core guided

Adv. Optical Mater. 2016, DOI: 10.1002/adom.201600171

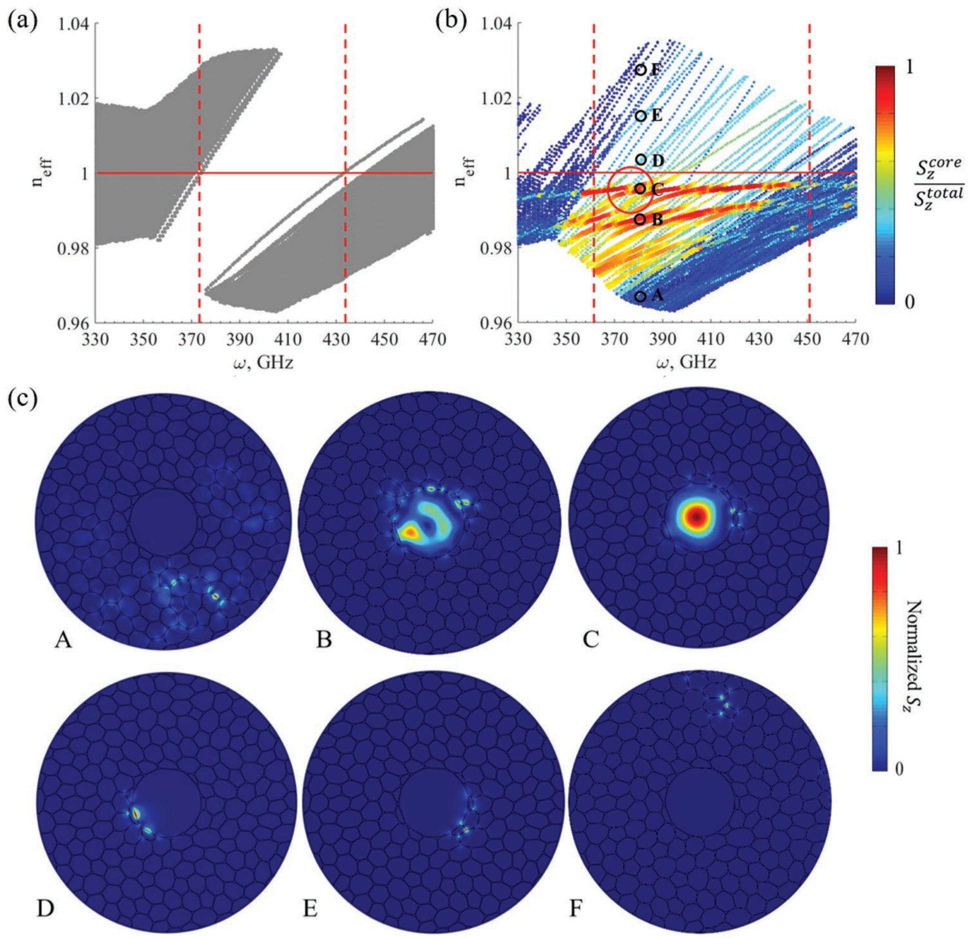

Figure 3. a) Band diagram of the numerically optimized reflector structure (a) without and (b) with the hollow core. Color of each dot indicates the fraction of power guided in the hollow core. The red circle highlights an example of the modal anticrossing between the fundamental core guided mode and one of the surface modes. The black circles refer to different types of modes guided by the waveguide at 0.38 THz. c) Normalized longitudinal flux of different modes labelled by black circles in (b). A and F: states of the reflector continuum located outside of the bandgap. B and C: second order core guided mode and fundamental core guided more located inside the bandgap. D and E: surface modes guided in the bandgap and localized in the immediate vicinity of the waveguide core/reflector interface.

modes in the reflector region. For example, in the vicinity of the core-guided mode C in Figure 2c ($n_{eff} = 0.9948$), we found a similar mode with orthogonal polarization with $n_{eff} = 0.9930$. Similarly, in the vicinity of the core guided mode B ($n_{eff} = 0.9961$), there is another mode with $n_{eff} = 0.9855$. By comparing the modal effective refractive indices, we estimate the birefringence of the core guided modes in our waveguide to be on the order of $\Delta n_{eff} \sim 1 \sim 2{\times}10^{-3}$.

Finally, for the sake of comparison, we now discuss modal structures for the two fabricated waveguides with bridge thicknesses of 200 and 250 µm. The corresponding band diagrams were calculated using the reflector geometries extracted from the high resolution photographs of the waveguides cross-sections [see Figure 1c,e], as well as using complex values of the reflector material refractive index [see Supporting Information Section 1]. As those waveguides feature suboptimal bridge and cylinder sizes, resultant bandgaps are smaller and positioned at lower frequencies (Figure 4c) than those of a fully optimized structure (see Figure 3b). For completeness, we also perform partial numerical optimization of the fabricated waveguides (Figure 4a) and compare their modal properties with those of the unoptimized fabricated waveguides. For example, during the partial optimization, the bridge thickness of a waveguide is fixed to 200 µm, which corresponds to the case of a fabricated waveguide presented in Figure 1c, while the cylinder diameter is changed until the optimal value is found. The optimal value is defined as one that results in the equidistant separation of the effective refractive index of the fundamental mode from both the lower and upper edges of the continuum of cladding states. Figure 4a depicts the partial optimization of the fabricated waveguide with the bridge thickness of 200 µm, where the cylinder diameter d_c is optimized to maximize the width of the bandgap centered at 365 GHz. The results show that when the cylinder diameter is 318 µm ($d_c/t_b = 1.59$), the dispersion relation of the fundamental guided mode is optimized according to the abovementioned criteria see (Figure 4b). In Figure 4b,c, we present the band diagrams of the partially optimized and experimental structures with 200 µm bridge thickness. The figures show strong similarity between the two band diagrams, as the relevant bandgaps feature similar central

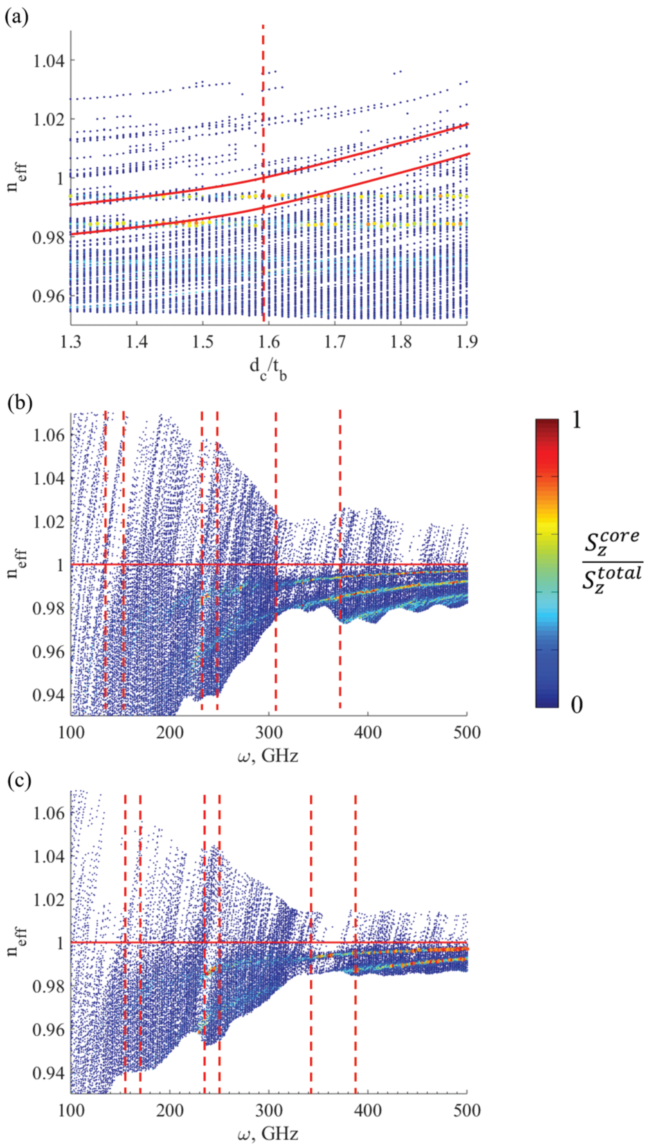

Figure 4. a) Partial optimization of the waveguide structure with a bridge thickness of 200 µm. Red solid lines refer to the boundaries of the reflector states, while the red dashed line indicates the optimal value of the cylinder diameter which maximizes the bandgap width. b) The band diagram of the partially optimized waveguide structure with a bridge thickness of 200 µm and cylinder diameter of 318 µm. c) The band diagram of the fabricated waveguide with bridge thicknesses of 200 µm.

frequencies and bandgap widths. Thus, we conclude that the experimental structure of the fabricated waveguide is close to the partially optimized one.

3.2. Waveguide Transmission Measurements

Next, we characterize THz transmission of the fabricated waveguides using a cut-back measurement, which is detailed in the Supporting Information [Section S2]. Transmission spectra of the fabricated waveguides with lengths of 2.5, 5.0, 7.5 and 10.0 cm are shown in **Figure 5**c,d. In order to calculate the bandgap width $\Delta\omega$, we applied the second moment method detailed in[23] with the full bandgap width defined as

$$\Delta\omega^2 = 4\frac{\int(\omega-\omega_c)^2 T(\omega)^2\, d\omega}{\int T(\omega)^2\, d\omega} \tag{3}$$

where ω_c is the bandgap central frequency and $T(\omega)$ is the field transmission. For the waveguide with a bridge thickness of 200 µm, there are four PBGs centered at frequencies of 0.17, 0.22 and 0.29 and 0.38 THz characterized by enhanced transmission. The spectral width of these PBGs are 18, 22, 44, and 49 GHz. Meanwhile, in the case of the waveguide with a bridge thickness of ≈250 µm, four bandgaps are centered at 0.14, 0.17, 0.23, and 0.29 THz, respectively. The estimated spectral widths of these bandgaps are 7, 25, 15, and 45 GHz. For comparison, in Figure 5a,b, we show the computed band diagrams for the fabricated waveguides with 200 and 250 µm bridge thicknesses. For the fabricated waveguide with a bridge thickness of 200 µm (see Figure 5a), three main bandgaps are centered at 0.14, 0.24, and 0.37 THz, with bandwidths of 13, 12, and 40 GHz, respectively, while for a waveguide with 250 µm bridge thicknesses, PBGs are discernable at 0.13, 0.24, and 0.33 THz with corresponding band widths of 20, 14, and 25 GHz. Overall, a relatively good agreement between the measured and theoretically predicted bandgap positions and sizes is achieved. Inconsistencies in the bandgap locations and sizes can be attributed to the conceptual differences between various approaches that are used to characterize the photonic bandgaps. Thus, when using band diagrams (Figures 5a,b), bandgap positions can, in principle, be inferred from the position of the "finger-like" spectral regions (see Discussion section) that do not support any reflector states, which is a classical definition of the bandgap in the case of waveguides. In practice, especially in the case of the multimode waveguides that support multiple core guided modes and surface states, unambiguous identification of such "finger-like" regions is problematic as clearly seen in Figures 5a,b. Moreover, from the same figures it is clear that dispersion relations of the core guided modes persist even outside of the bandgaps, thus resulting in relatively efficient transmission (albeit with higher losses) even outside of the bandgap regions. Therefore, one would expect some differences between classical definition of a bandgap from the structure of the modal band diagram as compared to the region of high transmission in the waveguide transmission spectrum. We note that there exists yet another approach to defining positions of the photonic bandgaps from the structure of the modal band diagram. In particular, one can plot the relative losses $\alpha(\omega)/\alpha_0(\omega)$ of all the modes (see Figures 5cd) and define bandgaps as spectral regions where modal losses of the core-guided modes are suppressed. Here, $\alpha_0(\omega)$ is the bulk material loss of the reflector material (see Figure S2 in the Supporting Information section). When compared to the actual transmission spectra shown in Figures 5e,f we note that a modal loss-based method offers a better match between the experimental transmission data and predictions based on numerical simulations.

Finally, we note that, as the light is guided in the hollow core, transmission losses of the fabricated waveguides can be expected to be significantly lower than those of the reflector

DOI: 10.1002/adom.201600171

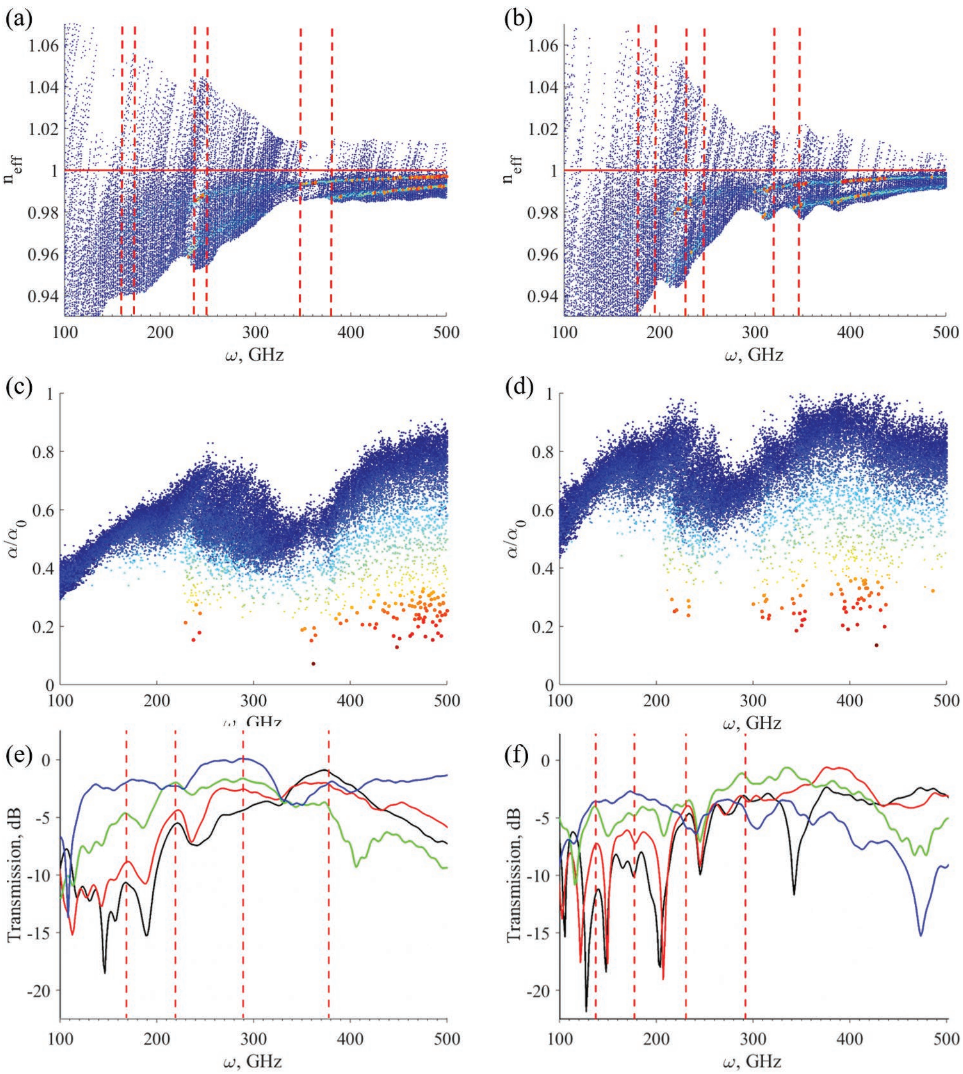

Figure 5. The simulated band diagrams of the fabricated waveguides with bridge thickness of a) 200 µm and b) 250 µm. c,d) the corresponding relative losses of all the modes of the two fabricated waveguides. The color code of the dots in (a–d) is the same as in Figure 4. Experimentally measured transmission spectra of the waveguide with e) 200 µm and f) 250 µm.

material. From Figure 5e,f, we can deduce the waveguide transmission loss in various bandgap regions by comparing transmission through waveguides of different lengths. In what follows, we use waveguides of 10 and 7.5 cm in our estimations. For instance, at 0.23 THz, the absorption loss of the first waveguide (t_b = 200 µm) is estimated to be ≈0.1 cm^{-1}, while that of the second waveguide (t_b = 250 µm) is ≈0.06 cm^{-1}. As expected, the propagation losses of the two fabricated waveguides are much smaller than the corresponding bulk absorption losses of the reflector material at the corresponding frequency, which is ≈0.55 cm^{-1} at 0.23 THz according to Equation (S2) (Supporting Information).

4. Discussion

First, we would like to clarify the definition of a bandgap in the context of our hyperuniform waveguides. We note that the definitions of a bandgap related to the quasi-3D photonic crystal fibers differ from that of 2D photonic crystal waveguides. In particular, for a 2D photonic crystal waveguide, one usually projects the full 3D band diagram along one direction (such as k_x in **Figure 6**a). Then, the region of frequencies that features no modes in the projected band diagram is defined as the complete bandgap of a 2D photonic crystal waveguide.[23] Such a bandgap is shown as an empty gray region in Figure 6a. However, in the case of the quasi-3D hollow-core photonic crystal fibers, complete bandgaps are rare, and one typically uses another definition of the bandgap, which is rather related to the position of the empty pockets of the modal phase space also known as "finger-like" regions (see Figure 6b). In this case, the edges of the bandgap are defined by the points of intersection of the air light line (n_a = 1) with the boundaries of the empty "finger-like" pockets in the band diagram as shown in Figure 6b, where the red dashed lines delimit the edges of the bandgap.[2] Within such defined bandgaps, the core guided

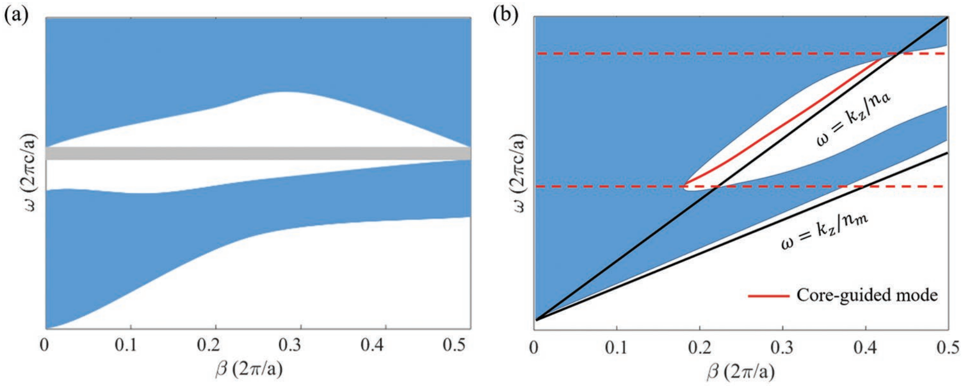

Figure 6. Schematic of the band diagram for a) 2D planar photonic crystal waveguides and b) quasi-3D photonic crystal fibers.

modes are well separated from the continuum of the cladding modes, and they propagate without scattering in the perfectly uniform waveguides. Generally, bandgap definition in the case of quasi-3D fibers results in much wider bandgaps compared to the size of complete bandgaps used in the case of 2D photonic crystal waveguides.

Next, we would like to compare transmission properties of our hollow-core waveguides that feature a hyperuniform cladding with other types of the hollow-core THz waveguides. In the **Table 1**, we present bandgap widths and transmission losses of several all-dielectric hollow-core photonic bandgap and antiresonant waveguides. The bandgap width is defined as the ratio of the full bandgap width to the bandgap central frequency (ω/ω_0). Our theoretically optimized waveguides feature a bandgap width of 21% at 0.41 THz, while the experimentally measured suboptimal waveguides feature a bandgap of 15.3% at 0.29 THz, which are comparable to the largest bandgaps reported for the photonic bandgap holey or Bragg fibers.[4–14] At the same time, it is not as wide as the spectral width of regions of high transmission featured by the antiresonant waveguides.[24–27] This is

Table 1. Comparison of the bandgap widths and losses of the hollow core fibers featuring different reflector types.

Fiber type	Reflector structure	Reflector material	Core diameter	Bandgap	Loss [cm^{-1}]	Reference
Hyperuniform fiber	Numerical optimized	Resin/air	≈5 mm	21% at 0.43 THz	–	–
	Fabricated	Resin/air	≈5 mm	15.3% at 0.29 THz	≈0.1 at 0.23 THz	–
Bragg fiber	All solid	PVDF/PC	≈1 mm	–	<0.02 at (1–3) THz	[4]
	Doped polymer	PE/PE with 80% wt. TiO_2	6.63 mm	≈13% at 0.68 THz	<0.042 at 0.69 THz	[5]
	Randomly porous layer	PE/air	6.73 mm	≈12% at 0.82 THz	<0.028 @ 0.82 THz	[7]
	Porous rings	PMMA/air	2 mm	–	<1.1 (1.0–1.6 THz)	[8]
	Cob-web structure	HDPE/air	16 mm	–	5.84×10^{-8} at 0.55 THz	[9]
Holey fiber	Rectangular lattice	PTFE/air	1.12 × 1.87 mm	≈20% at 1.66 THz for $d/\Lambda = 0.96$	–	[11]
	Hexagonal lattice with regular holes	HDPE/air	292 µm	≈7.5% at 1.47 THz for $d/\Lambda = 0.93$;	≈0.022 at 1.53 THz for $d/\Lambda = 0.93$;	[12]
				≈14% at 1.66 THz for $d/\Lambda = 0.93$	≈0.014 at 1.75 THz for $d/\Lambda = 0.96$;	
	Hexagonal lattice with inflated holes	Teflon/air	840 µm	≈17% at 1.80 THz	<0.04 cm^{-1} at (1.65–1.95) THz	[11]
	Honeycomb	Topas/air	≈1 mm	≈4% at 0.98 THz	≈0.058 at 0.98 THz	[13]
ARROW fiber	Hollow core tube	PTFE	≈8.24 mm	≈41% at 1.25 THz for 0.3 mm thin tube	–	[23]
	Kagome	PMMA/air	1.6 mm	≈28% at 0.87 THz	<0.1 at (0.75–1) THz	[28]
			2.2 mm	≈45% at 0.77 THz	<0.06 at (0.65–1 THz)	
	Tube (Single ring)	PMMA/are	1.62 mm	≈23% at 0.85 THz	≈0.04 at 0.83 THz	[24]
	Tube (Several rings)	PE/air	5.5 mm	≈8% at 0.49 THz	–	[25]

DOI: 10.1002/adom.201600171

to be expected as in the case of antiresonant waveguides the concept of "bandgap" is not strictly defined, and their transmission spectra do not manifest an abrupt transition from guided to non-guided regimes when crossing the bandgap boundaries. We also believe that hyperuniform fibers can be further optimized to result in larger bandgaps via exploration of other point patterns. Thus, further work is still necessary to find out the maximal bandgap size possible with hyperuniform disordered reflectors.

As it can be seen in Table 1, the measured losses of our hyperuniform fiber are higher than those of other types of photonic bandgap fibers. This phenomenon has multiple causes. First, due to requirements of the fabrication process, we use a highly absorbent polymer (VisyJet Crystal) as the reflector material that features material absorption that is much higher than that of other commercial polymers normally used for THz fibers, such as polyvinylidene fluoride (PVDF), polycarbonate (PC), polyethylene (PE), poly(methyl methacrylate) (PMMA), polytetrafluoroethylene (PTFE), etc. High absorption of the reflector material results in high losses of both the core-guided and the cladding modes. Second, our fiber features many surface states that are bound to the core/reflector interface and, thus, exhibit significant presence in the lossy cladding material [see modes D and E in Figure 3c]. Over a certain frequency range, these surface modes hybridize with the core-guided modes and eventually "transform" into the core-guided modes, and vice versa.[29] This phenomenon is known as anticrossing (or avoided crossing) and is presented schematically in **Figure 7**a. Owing to the anticrossing phenomenon, both the dispersion relations and the losses of the core-guided modes can be significantly altered in this frequency range. In Figure 7b,c, we present modal properties in the spectral region of anticrossing between the core guided mode and one of the surface states. Near 375 GHz, the fundamental mode (black circles) shows strong hybridization with a surface state (blue circles), thus leading to a significant increase in the losses of a core guided mode. As seen in Figure 3b, due to a large number of the surface states, one, therefore, expects the overall loss increase in the propagation losses of the core guided modes due to their interaction with surface states.

Finally, we would like to comment on the 3D MultiJet printing technique that has been used in this paper. Overall, this is a mature technology that has been widely used in the fabrication of microelectronic and optical devices.[30–33] Currently, ≈200 µm lateral resolution is standard, while some commercial system also offers sub 50 µm lateral resolution. The biggest limitations of this technology are a limited material choice (photosensitive resins used in fabrication), model geometry and limited build volumes (≈10–20 cm linear dimension). Compared with the traditional fiber drawing fabrication method even when supplemented with stacking method,[27] drilling method,[34] and extrusion moulding method[35] for preform fabrication, the 3D MultiJet printing technology still enables fabrication of waveguides with significantly more complex transverse profile. At the same time, fiber drawing does not suffer from "resolution" issues that are present in 3D printing, thus enabling fabrication of long (tens of meters), very smooth, submicron-thin THz structures.

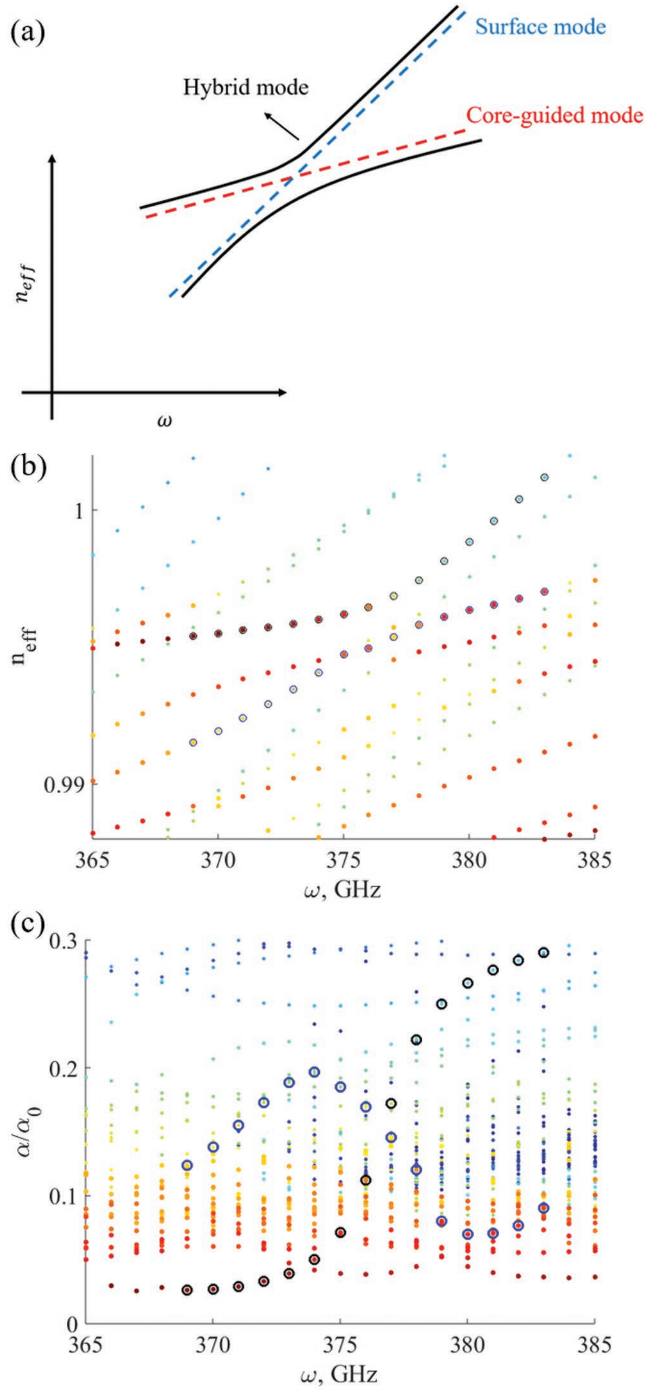

Figure 7. a) Schematic of the modal anticrossing of the core-guided mode (red dashed line) and the surface mode (blue dashed line). The black solid lines refer to the dispersion relations of the hybridized modes. b) Dispersion relations and c) losses of the modes in the area highlighted by the red circle in Figure 3b. Two hybridized modes are labeled by black circles and blue circles, respectively. The color code of (b) and (c) are the same as that shown in Figure 3.

5. Conclusion

Hollow core waveguides featuring a hyperuniform disordered reflector in the cladding are proposed for applications in the terahertz frequency range. The reflector consists of the disorderly positioned dielectric cylinders that are connected with thin dielectric bridges. Center positions of the cylinders follow a hyperuniform disordered point pattern with the hyperuniformity parameter χ equal to 0.5. The proposed reflector structure was further optimized to maximize the photonic bandgap in the vicinity of 0.4 THz, and the optimal bridge thickness and the cylinder diameter were found to be 35 and 113 µm, respectively. The resulting photonic bandgap features a full width of 90 GHz (≈21%).

Based on the numerically optimized waveguide structure, two hollow core waveguides with different bridge thicknesses were fabricated using a commercial 3D MultiJet printer. Due to limitations of the printing process, the resultant waveguides featured much wider bridge thickness (200 and 250 µm), while having the same overall structure of the reflector. We then theoretically investigated modal properties of the fabricated waveguides using a finite element method. Because of the suboptimal bridge thicknesses used in these waveguide, they exhibit smaller photonic bandgaps (≈15%) when compared to those of the optimal structure. Finally, we performed optical characterization of the two fabricated waveguides using a modified THz-TDS system. For the fabricated waveguide with the bridge thickness of 200 µm, spectral regions of enhanced transmission (bandgaps) are located at 0.17, 0.22 and 0.29 and 0.38 THz, and the corresponding spectral widths are 18, 22, 44 and 49 GHz, respectively, resulting in a maximum bandgap of ≈15.1% at 0.29 THz. When the bridge thickness is increased to 250 µm, central frequencies of these bandgaps are shifted to 0.14, 0.17, 0.23, and 0.29 THz, respectively, and the corresponding spectral widths are reduced to 7, 25, 15, and 45 GHz. The maximum bandgap of this waveguide is measured to be ≈15.3% at 0.29 THz. The location and the widths of the experimentally measured bandgaps are in agreement with the theoretical predictions. Moreover, due to hollow core guidance, transmission losses (within the bandgap) of the fabricated waveguides are significantly smaller than the bulk absorption loss of the reflector material.

6. Experimental Section

Fiber Fabrication: The developed waveguides shown in this paper were fabricated using a commercial MultiJet 3D printer (ProJet 3500HD Plus) with the photoresin (VisyJet Crystal). In order to print robust structures, the minimum dielectric bridge thickness is required to be at least four times of the printer resolution, namely ≈200 µm. Hence, we could not print the waveguide with the optimized structure. Instead of the optimized structure, we, therefore, printed two types of waveguides with bridge thicknesses of 200 and 250 µm, respectively, while keeping the same distribution of cylinders. For each waveguide, we printed four sections with lengths of 25 mm each. As we used the same drawing file for the printing, these two waveguides have almost the same reflector size with ≈22 mm outer diameter and ≈5 mm diameter hollow core. The cross-section of the fabricated waveguides is illustrated in Figure 1c,e.

Supporting Information

Supporting Information is available from the Wiley Online Library or from the author.

Received: March 11, 2016
Revised: July 25, 2016
Published online:

[1] E. Yablonovitch, *Phys. Rev. Lett.* **1987**, *58*, 2059.
[2] P. J. Russell, *J. Lightwave Technol.* **2006**, *24*, 4729.
[3] F. Gérôme, R. Jamier, J. Auguste, G. Humbert, J. Blondy, *Opt. Lett.* **2010**, *35*, 1157.
[4] M. Skorobogatiy, A. Dupuis, *Appl. Phys. Lett.* **2007**, *90*, 113514.
[5] A. Dupuis, K. Stoeffler, B. Ung, C. Dubois, M. Skorobogatiy, *J. Opt. Soc. Am. B* **2011**, *28*, 896.
[6] B. Ung, A. Dupuis, K. Stoeffler, C. Dubois, M. Skorobogatiy, *J. Opt. Soc. Am. B* **2011**, *28*, 917.
[7] A. Hassani, A. Dupuis, M. Skorobogatiy, *Opt. Express* **2008**, *16*, 6340.
[8] C. S. Ponseca, R. Pobre, E. Estacio, N. Sarukura, A. Argyros, M. C. J. Large, M. A. van Eijkelenborg, *Opt. Lett.* **2008**, *33*, 902.
[9] R. J. Yu, B. Zhang, Y. Zhang, C. Wu, Z. Tian, X. Bai, *IEEE Photonics Technol. Lett.* **2007**, *19*, 910.
[10] S. Atakaramians, S. Afshar, H. Ebendorff-Heidepriem, M. Nagel, B. M. Fischer, D. Abbott, T. M. Monro, *Opt. Express* **2009**, *17*, 1405.
[11] G. Ren, Y. Gong, P. Shum, X. Yu, J. Hu, *IEEE J. Quan. Elec.* **2009**, *45*, 506.
[12] A. Barh, R. Varshney, B. Pal, G. Agrawal, A. Rahma, in *12th Int. Conf. on Fiber Optics and Photonics, OSA Technical Digest*, OSA Publishing, Washington DC **2014**, T2D.6.
[13] K. Nielsen, H. Rasmussen, P. Jepsen, O. Bang, *Opt. Lett.* **2011**, *36*, 666.
[14] M. Florescu, S. Torquato, P. J. Steinhardt, *Proc. Natl. Acad. Sci.* **2009**, *106*, 20658.
[15] K. Vynck, M. Burresi, F. Riboli, D. S. Wiersma, *Nat. Mater.* **2012**, *11*, 1017.
[16] T. Amoah, M. Florescu, *Phys. Rev. B* **2015**, *91*, 020201.
[17] W. Man, M. Florescu, E. P. Williamson, Y. He, S. R. Hashemizad, B. Y. C. Leung, D. R. Liner, S. Torquato, P. M. Chaikin, P. J. Steinhardt, *Proc. Natl. Acad. Sci.* **2013**, *110*, 15886.
[18] W. Man, M. Florescu, K. Matsuyama, P. Yadak, G. Nahal, S. Hashemizad, E. Williamson, P. Steinhardt, S. Torquato, P. Chaikin, *Opt. Express* **2013**, *21*, 19972.
[19] S. Tsitrin, E. P. Williamson, T. Amoah, G. Nahal, H. L. Chan, M. Florescu, W. Man, *Sci. Rep.* **2015**, *5*, 13301.
[20] R. D. Batten, F. H. Stillinger, S. Torquato, *J. Appl. Phys.* **2008**, *104*, 033504.
[21] S. Torquato, F. H. Stillinger, *Phys. Rev. E* **2003**, *68*, 041113.
[22] S. G. Johnson, M. Ibanescu, M. Skorobogatiy, O. Weisberg, T. D. Engeness, M. Soljacic, S. A. Jacobs, J. D. Joannopoulos, Y. Fink, *Opt. Express* **2001**, *9*, 748.
[23] M. Naftaly, *IEEE Sensors J.* **2013**, *13*, 8.
[24] A. E. Siegman, in *Proc. Diode Pumped Solid State Lasers: Applications and Issues*, OSA Publishing, Washington DC **1997**, MQ1.
[25] B. Ung, A. Mazhorova, A. Dupuis, M. Rozé, M. Skorobogatiy, *Opt. Express* **2011**, *19*, B848.
[26] J. Anthony, R. Leonhardt, S. Leon-Saval, A. Argyros, *Opt. Express* **2011**, *19*, 18470.
[27] V. Setti, L. Vincetti, A. Argyros, *Opt. Express* **2013**, *21*, 3388.
[28] M. Skorobogatiy, J. Yang, Cambridge University Press, Cambridge, UK **2009**.
[29] J. Li, H. Qu, M. Skorobogatiy, *Opt. Express* **2016**, *24*, 15687.
[30] J. Lu, C. Yu, H. Chang, H. Chen, Y. Li, C. Pan, C. Sun, *Appl. Phys. Lett.* **2008**, *92*, 064105.
[31] S. Wu, C. Yang, W. Hsu, L. Lin, *Microsys. Micro. Eng.* **2015**, *1*, 1501310.
[32] S. Pandey, B. Gupta, A. Nahata, *Opt. Express* **2013**, *21*, 24422.
[33] N. Yudasari, J. Anthony, R. Leonhardt, *Opt. Express* **2014**, *22*, 26042.
[34] T. Ma, A. Markov, L. Wang, M. Skorobogatiy, *Opt. Express* **2015**, *23*, 7856.
[35] J. Wang, X. H. Yang, L. L. Wang, *Opt. Express* **2008**, *16*, 7703.